## RESEARCH ARTICLE

**Key Points:**
- Standard fluvial failure models are mostly developed as empirical approximations of observation on frontal dike failure (dam configuration)
- Peculiarities of the flow in the main channel must be accounted for in the prediction of the dike breach evolution
- The dynamics of the deepening, upward widening, and downward widening of the breach are underpinned by different physical processes

**Correspondence to:**
I. Rifai,
I.Rifai@doct.ulg.ac.be

# Overtopping induced failure of noncohesive, homogeneous fluvial dikes

Ismail Rifai[1,2] (ID), Sebastien Erpicum[1] (ID), Pierre Archambeau[1] (ID), Damien Violeau[2], Michel Pirotton[1] (ID), Kamal El Kadi Abderrezzak[2] (ID), and Benjamin Dewals[1] (ID)

[1]ArGEnCo Department, Research Group Hydraulics in Environmental and Civil Engineering, University of Liège, Liège, Belgium, [2]EDF R&D, National Laboratory for Hydraulics and Environment, and Saint Venant Laboratory for Hydraulics, Chatou, France

**Abstract** Accurate predictions of breach characteristics are necessary to reliably estimate the outflow hydrograph and the resulting inundation close to fluvial dikes. Laboratory experiments on the breaching of fluvial sand dikes were performed, considering a flow parallel to the dike axis. The breach was triggered by overtopping the dike crest. A detailed monitoring of the transient evolution of the breach geometry was conducted, providing key insights into the gradual and complex processes involved in fluvial dike failure. The breach develops in two phases: (1) the breach becomes gradually wider and deeper eroding on the downstream side along the main channel and (2) breach widening controlled by side slope failures, continuing in the downstream direction only. Increasing the inflow discharge in the main channel, the breach formation time decreases significantly and the erosion occurs preferentially on the downstream side. The downstream boundary condition has a strong influence on the breach geometry and the resulting outflow hydrograph.

## 1. Introduction

Fluvial dikes (i.e., earthen levees along river banks) have been built to prevent lateral riverbed migration, channelize the flow, and as defense structures to protect humans and property from inundations. They are composed of different material ranging from cohesive (e.g., Lower Rhine River, Lower Rhone River, and its delta) to noncohesive sediments (e.g., Upper Rhone River, Upper Saone River, Missouri River). Lack of maintenance, inadequate rehabilitation works (e.g., grass cover and tree roots poorly managed), wildlife activity (e.g., animal burrows) [*Orlandini et al.*, 2015], and exposure to frequent events (e.g., high water levels, riverbed changes) [*Apel et al.*, 2009; *Hui et al.*, 2016] increase dike vulnerability, which may lead to subsequent failure disasters. Overtopping has been identified as the main cause of failure [*Vorogushyn et al.*, 2010; *Fry et al.*, 2012], occurring typically if the river discharge exceeds the design value of the dike during a flood event or, broadly, if the water level exceeds the dike crest or the flow overtops a weak dike segment. These scenarios will typically occur in the near future, because extreme hydrological events are expected to become more frequent [*Madsen et al.*, 2014; *IPCC*, 2014].

Accurate predictions of the breach geometry and outflow hydrograph are important to estimate the inundation extent, to plan emergency operations and to design mitigating measures. However, the current knowledge on the physical processes underpinning fluvial dike failure due to overtopping remains limited. The breach process has been often assessed using standard models, mostly developed empirically from frontal dike (i.e., dam) configurations. An extensive review of empirically based models is given by *Wahl* [2004] and *ASCE/EWRI Task Committee on Dam/Levee Breaching* [2011]. These models ignore the specific boundary conditions and flow features related to the fluvial configuration [*Roger et al.*, 2009]; their application to field cases remains therefore questionable [*Morris et al.*, 2009; *Wahl and Lentz*, 2012]. The existing knowledge on dam and dike breaches originates from statistical analyses of historical data [e.g., *Singh*, 1996; *Froehlich*, 2008; *Jandora and Říha*, 2008], numerical modeling [e.g., *Wu et al.*, 2012; *Nakagawa et al.*, 2013; *Dou et al.*, 2014; *Kakinuma and Shimizu*, 2014], and from small-scale laboratory experiments. The present study focuses on this approach.

Most existing breach experiments disregarded the flow parallel to the dike axis. Either overtopping was simulated by rising the upstream water level above the entire dike crest (i.e., plane erosion) or above an initial

**Table 1.** Experimental Setups of Selected Studies on Spatial Dike Erosion due to Overtopping

| Reference | Setup | Scale | Dike Material | Inflow Conditions (Reservoir Water Level) |
|---|---|---|---|---|
| *Simmler and Samet* [1982] | | | Noncohesive/cohesive | Falling |
| *Pugh* [1985] | Frontal | Lab | Noncohesive/cohesive | Constant |
| *Coleman et al.* [2002] | | | Noncohesive | Constant |
| *Rozov* [2003] | | | Cohesive | Falling |
| *Chinnarasri et al.* [2004] | | | Noncohesive | Falling |
| *Spinewine et al.* [2004] | | | Noncohesive | Falling |
| *Orendorff et al.* [2013] | | | Noncohesive | Falling |
| *Zhu et al.* [2011] | | | Cohesive | Constant |
| *Pickert et al.* [2011] | | | Cohesive | Constant |
| *Al-Riffai* [2014] | | | Noncohesive | Falling |
| *Frank and Hager* [2015] | | | Noncohesive | Falling |
| *Tabrizi et al.* [2016] | | | Noncohesive | Falling |
| *Visser* [1998] | | Lab and prototype | Noncohesive | Constant/falling |
| *Morris et al.* [2007] | | | Noncohesive/cohesive | Constant/falling |
| *Powledge et al.* [1989] | | Prototype | Noncohesive/cohesive | Falling |
| *Zhang et al.* [2009] | | | Cohesive | Falling |
| *Islam* [2012] | | | Noncohesive/cohesive | Falling |
| *Michelazzo* [2014] | | | Noncohesive | Falling |
| *Bhattarai et al.* [2015] | | Lab | Cohesive | Falling |
| *Charrier* [2015] | Fluvial | | Cohesive | Falling |
| *Tabrizi et al.* [2015] | | | Noncohesive | Falling |
| *Wei et al.* [2016] | | | Cohesive | Falling |
| *Kakinuma and Shimizu* [2014] | | Prototype | Noncohesive/cohesive | Falling |

notch located along the dike crest (i.e., spatial erosion) [*Schmocker*, 2011]. For the plane case, erosion of the dike profile is uniform along the dike crest axis. The dynamics of breach widening is then ignored. Spatial erosion includes both breach deepening and widening, representing in a more realistic way dike breach processes [*Frank and Hager*, 2015]. Table 1 reports selected spatial erosion cases. Experimental studies on frontal configurations are numerous [*Rifai et al.*, 2015], covering breach development and shape, effects of upstream water level (e.g., falling or constant), dike material (e.g., cohesion, grain size diameter, compaction, water content) as well as dike reinforcements. On the contrary, those on fluvial dike configurations remain fragmented, with subsisting discrepancies in the outcomes [*Rifai et al.*, 2016a]. In addition, there is a lack of a continuous monitoring of the 3-D breach formation, limiting the analysis of the key mechanisms governing breach development and the use of data for the assessment of numerical or parametric models. Hence, more research efforts focusing on fluvial configurations are required to fully grasp the signature of the prevailing flow structures on the breach mechanisms.

The present study addresses these topics by performing laboratory tests on breach formation of homogeneous, noncohesive fluvial dikes due to overtopping, without grass cover and outer protection. A well-documented, reliable data set with a continuous high resolution monitoring of the 3-D breach evolution under various flow conditions is provided. These two aspects are relevant to assess parametric breach models and numerical codes. The present experiments are part of a broader research work including additional tests with different channel, floodplain, and dike dimensions as well as dike material and reinforcement. The paper is organized as follows: section 2 describes the experimental setup and test program. In section 3, the monitoring strategy for the 3-D breach development is detailed, particularly a laser profilometry technique. Results are analyzed in section 4, followed by concluding remarks in section 5.

## 2. Experimental Model

### 2.1. General Setup

The laboratory experiments were conducted at the Engineering Hydraulics Laboratory of the University of Liège. The present set of experiments was not a scaling of a specific field dike. The flume (i.e., main channel) was $L_{mc} = 10$ m long and $l_{mc} = 1$ m wide, straight and open on one side (Figure 1). The water intake tank was separated from the flume by a honeycomb straightener. The flume dike side was open over 3 m toward a 4.3 m × 2.5 m floodplain. This side opening was covered with sand to represent the fluvial dike (see section 2.2). The flume and floodplain were covered with impermeable whitewash coatings to ensure
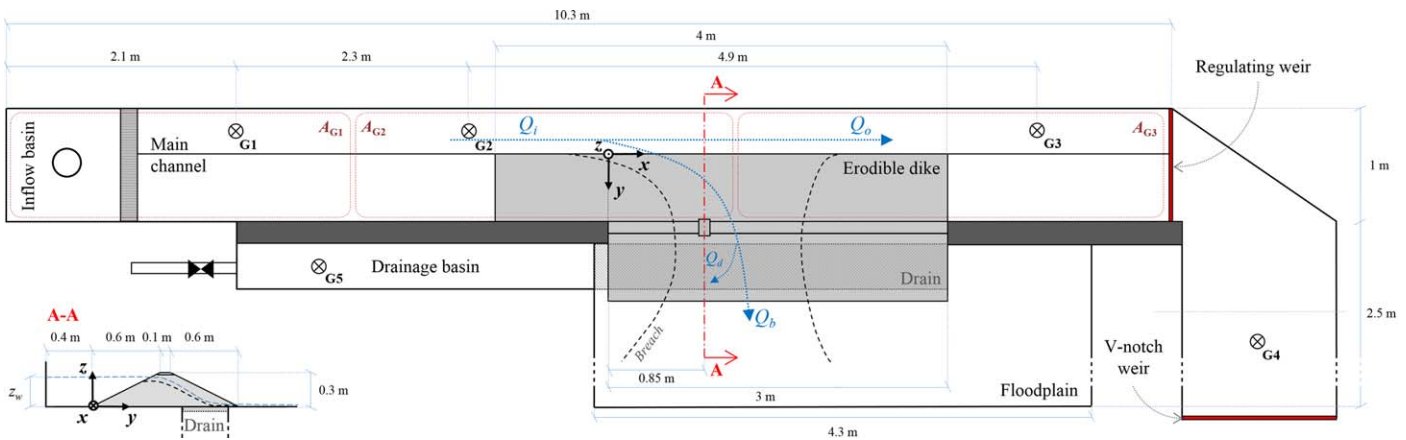
**Figure 1.** Setup plan view and dike cross section.

roughness continuity between the flume, floodplain and sand dike. The flume and floodplain were at the same level. The whole model was elevated by 0.70 m so that water across the breach was freely discharged from the floodplain without any storage change or tail water effects. To ensure the dike stability prior to overtopping, the seepage flow was limited by installing a drainage system at the dike bottom (Figure 1). The drainage system consisted of a 4 cm-thick layer of dike material wrapped in a geotextile that was placed on a coarse grid. The seepage flow through the dike was collected in a reservoir and the drainage discharge $Q_d$ was measured.

The dike was $L_d = 3$ m long, $h_d = 0.3$ m high and of trapezoidal shape. The crest was $l_{dc} = 0.1$ m wide and the inner and outer dike face slopes were $S_i = S_o = 1{:}2$ (V:H); the total dike width was $l_d = 1.3$ m. A 0.02 m deep and 0.1 m wide initial notch was cut into the crest 0.8 m far from the upstream end of the sand dike (Figure 1). The dike was composed of noncohesive, uniform sand of median diameter $d_{50} = 1$ mm and sorting coefficient $\sigma = (d_{84}/d_{50} + d_{50}/d_{16})/2 = 1.22$, with $d_{16} = 0.84$ mm and $d_{84} = 1.24$ mm. The median diameter was in the range between 1 and 5.5 mm, as recommended by *Schmocker and Hager* [2012] to prevent excessive seepage and scale effects. The sand had a density $\rho_s = 2500$ kg/m$^3$, a bulk density $\rho_b = 1600$ kg/m$^3$ and a porosity $p = 0.36$.

### 2.2. Test Program

A total of 17 tests are presented (Table 2). The inflow discharge in the main channel $Q_i$ was kept constant in the range between 0.02 and 0.057 m$^3$/s, corresponding to inlet Froude numbers $\mathbf{F}_i = [l_{mc} \times Q_i^2/(A_{mc}^3 \times g)]^{0.5}$ in the range of 0.066–0.189, with $A_{mc}$ the channel flow cross-sectional area and $g$ the gravity acceleration. Repeatability and reliability of measurements were checked by performing three identical experiments (Tests 6–8). The breach development was found to be similar.

In most tests, a perforated plane located at the downstream end regulated the flow. This system with evenly distributed holes allowed for a quasi-uniform velocity distribution over the cross section. For a given inflow discharge $Q_i$, the number of holes and their arrangement were selected to ensure that the water level in the main channel was at the dike crest level. Additional tests were performed using two other regulating systems, a rectilinear weir and a

**Table 2.** Test Configurations

| Test No. | $Q_i$ (m$^3$/s) | $\mathbf{F}_i$ | Downstream Boundary Condition |
|---|---|---|---|
| 1 | 0.020 | 0.066 | Perforated plane |
| 2 | 0.021 | 0.070 | |
| 3 | 0.028 | 0.093 | |
| 4 | 0.030 | 0.100 | |
| 5 | 0.031 | 0.103 | |
| 6 | 0.040 | 0.133 | |
| 7 | 0.040 | 0.133 | |
| 8 | 0.040 | 0.133 | |
| 9 | 0.041 | 0.136 | |
| 10 | 0.047 | 0.156 | |
| 11 | 0.050 | 0.166 | |
| 12 | 0.051 | 0.169 | |
| 13 | 0.055 | 0.182 | |
| 14 | 0.057 | 0.189 | |
| 15 | 0.041 | 0.136 | Sluice gate |
| 16 | 0.042 | 0.139 | Rectilinear weir |
| 17 | 0.040 | 0.133 | |

sluice gate (Table 2). The rating curves are provided as supporting information. The influence of the downstream regulating system is discussed in section 4.3.

### 2.3. Test Procedure

The dike was placed by staking and compacting manually the sand to avoid any structural defect. A template of the trapezoidal cross section was then swiped along the longitudinal axis (i.e., $x$ axis) to shape the dike and remove excess material, before setting the initial notch. For Tests 1–15, the main channel was filled progressively with a discharge $Q_{i0}$ equal to about 75% of the test inflow discharge $Q_i$. For Tests 16 and 17 (i.e., rectilinear weir), $Q_{i0} \approx 0.5 \times Q_i$ to avoid overtopping the initial notch. Once the flow had stabilized, the dike and drainage system were first inspected and the inflow discharge was then increased to $Q_i$. The water level in the main channel increased and overtopped the dike over the initial notch, thereby resulting in a subsequent breach process. Tests were stopped when one of the breach sides met the rigid wall of the flume.

## 3. Measurement Techniques

### 3.1. Water Level and Flow Discharge Monitoring

Using ultrasonic sensors of $\pm1\%$ accuracy (mic+35/IU/TC by Microsonic), the water level was measured at three gauge stations in the main channel, G1, G2, and G3 and upstream of the V notch weir (G4) (Figure 1). The inflow discharge $Q_i$ was measured using an electromagnetic flowmeter of $\pm0.4\%$ accuracy (Siemens MAG 5000W). The outflow discharge $Q_o$ was estimated from the discharge passing through the V notch weir (deduced from water level at G4) and the mass balance in a control volume located between the regulating and V notch weirs. A comparison between the computed outflow discharges and those deduced from the rating curve of the perforated plane showed that maximum deviation was below 10% of $Q_i$, whereas the root mean square error represented 3.5% of $Q_i$. The drained flow was collected in a reservoir located below the dike. The drainage discharge $Q_d$ was deduced from the water level evolution measured at G5. Overall, $Q_d$ was limited at 2 L/s at the test start and at 1.2 L/s for the remaining test duration. The breach discharge $Q_b$ was deduced from the following mass balance (Figure 1):

$$Q_b = Q_i - Q_o - Q_d - (A_{G1} + A_{G2} + A_{G3})\frac{dz_w}{dt} \tag{1}$$

here $t$ is time and $z_w = (A_{G1}z_{G1} + A_{G2}z_{G2} + A_{G3}z_{G3})/(A_{G1} + A_{G2} + A_{G3})$ a weighted average of water levels $z_{G1}$, $z_{G2}$, and $z_{G3}$ at G1, G2, and G3, respectively, with $A_{G1}$, $A_{G2}$, and $A_{G3}$ as main channel surface areas associated with G1, G2, and G3, respectively (Figure 1).

### 3.2. Breach Evolution Monitoring

A nonintrusive laser profilometry technique was developed to record the breach development. The laser profilometry was performed with a red diode of 30 mW laser of 75° fan angle (Z-Laser Z30M18S3-F-640-LP75). The swiping was ensured by rotating the laser with a stepper motor; one complete dike swiping lasted about 1.5 s. The recording was performed by a digital video camera. The acquisition was set to Full-HD resolution (1920 × 1080 pixels) and a recording speed of 60 frames/s. Each complete reconstruction was based on about 90 profiles. The combination of all profiles from a complete swiping allowed for a restitution of a cloud of points in the object coordinates. Details of the breach geometry reconstruction are given by *Rifai et al.* [2016b].

Because the dike was partially under water during an experiment (Figure 2), the projected laser sheet was refracted when passing the water surface and rays from the laser profile to the camera were refracted when entering the air medium. This caused a deformed image and an inaccurate definition of the laser plane. To correct this feature, the Snell-Descartes law [*Glassner*, 1989] was used, in which the water surface in the channel was assumed horizontal and the flow surface across the breach was approximated as an inclined plane. Despite these simplifying assumptions regarding the water surface in the vicinity of the breach, the refraction correction highly improved the results (Figures 2d and 2e).
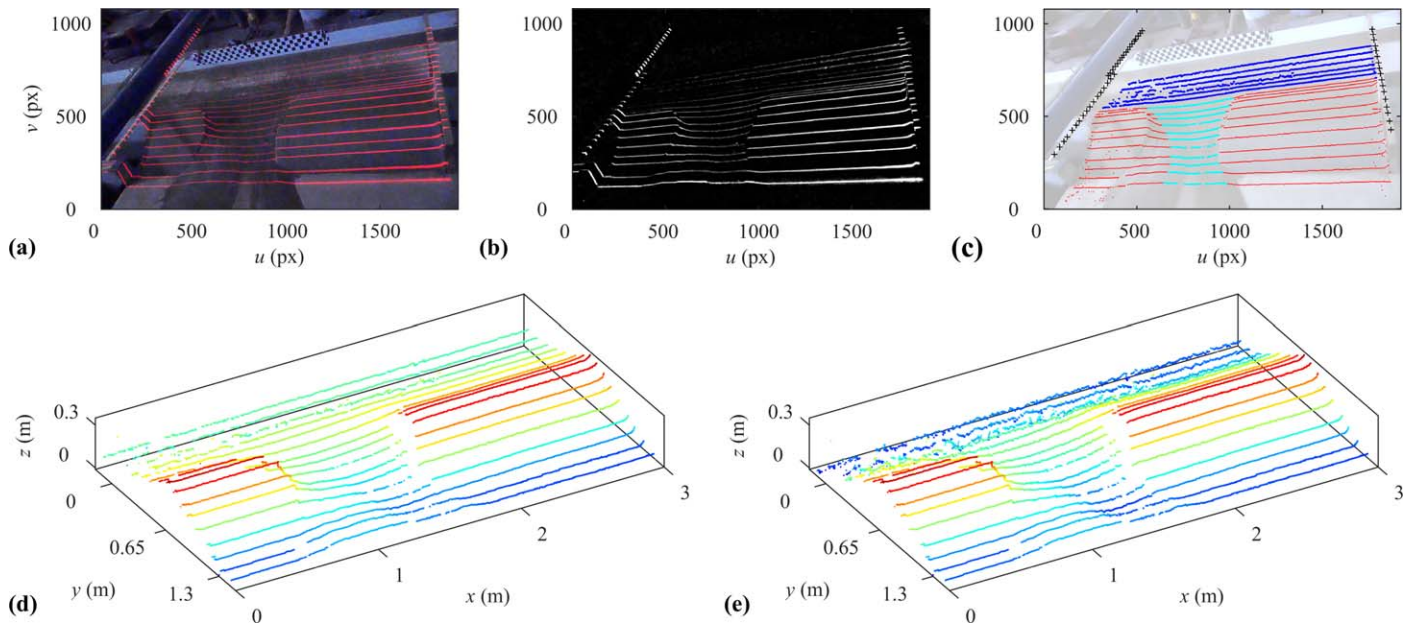
**Figure 2.** 3-D dike geometry reconstruction: (a) raw images, (b) filtered images, (c) detection of laser profiles and identification of submerged zones, (d) 3-D raw reconstruction, and (e) corrected 3-D reconstruction.

## 4. Results

### 4.1. General Observations

#### 4.1.1. Breach Evolution

In the following sections, "upstream" and "downstream" refer to the upstream and downstream sides along the channel, respectively, while "channel side" and "floodplain side" refer to the upstream and downstream breach sides, respectively. The initial time is set when the water level in the main channel reaches the downstream portion of the initial notch. The qualitative description of the breaching process presented hereafter is valid for all laboratory tests listed in Table 2. For the sake of brevity, results are shown for Test 8 only. The numerical values mentioned here below are specific to Test 8.

Erosion of the initial notch is triggered with flow overtopping (Figure 3). During the early stage ($t \leq 27$ s), the erosion rate is relatively slow because the overtopping flow depth remains small; the eroded material from the upper part is deposited at the dike toe. As the overtopping flow depth becomes larger ($27 \leq t \leq 210$ s), the erosion process across the dike is accelerated, leading to combined deepening and widening of the breach and a shifting of the breach centerline toward downstream of the channel. This behavior underlines the significant influence of the momentum component parallel to the dike crest [*Roger et al.*, 2009]. The typical *hour glass* shape is observed, losing, however, its symmetry as the breach expands. At $t \geq 210$ s, the dike geometry upstream of the breach stops evolving and the breach widens along the channel flow direction only (Figure 4a). The breach development becomes slower during this phase because the water level in the main channel decreases. Some material is eroded from the breach bottom and deposited near the downstream channel side (Figure 3, $t \geq 660$ s).

Figures 4b–4g depict the contrasting evolution of different dike cross sections. At the initial notch ($x = 0.85$ m), a significant erosion of the dike channel side is observed, caused by flow acceleration upstream of the breach. At $x = 1.2$ and 1.55 m, erosion occurs mainly on the floodplain side of the dike, resulting in its collapse around a *pivot point*. This is similar to observations by *Coleman et al.* [2002] and *Schmocker* and *Hager* [2009] for frontal dike configurations. Once the channel bottom is reached ($t = 210$ s), the breach widening continues due to slope failure of the dike floodplain side. This is shown at $x = 1.90$ m (Figure 3e), highlighting that the entire trapezoidal dike shape has dropped by few centimeters.

The subsequent breach widening results from slope failure and erosion of the collapsed material by the breach flow (Figures 4f and 4g). During the experiments (see video in supporting information), the breach evolves first gradually as sand material is eroded and transported mainly via bed load. As the flow in the
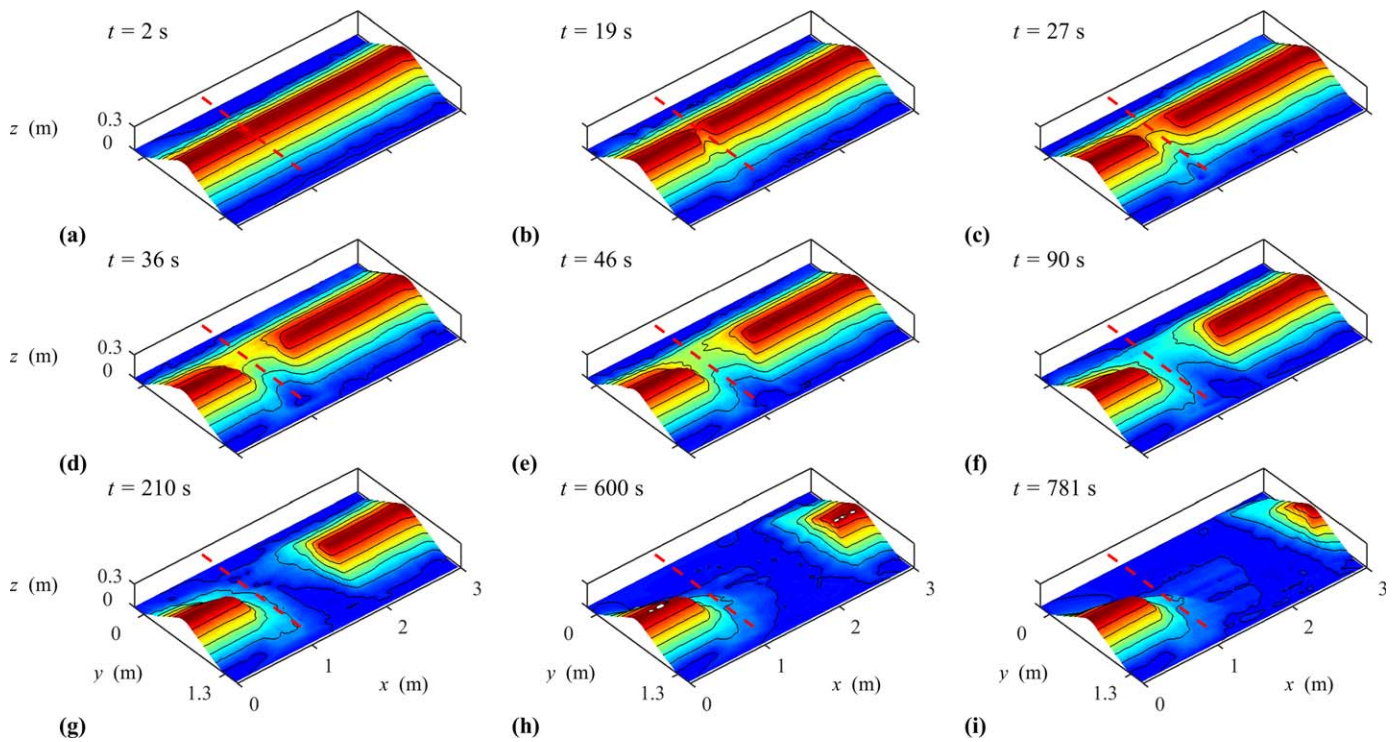
**Figure 3.** Reconstructed breach topography for Test 8. Dashed lines indicate position of the initial notch.

main channel accelerates, erosion becomes more concentrated toward the channel side (right side in Figure 4a), causing erosion of the breach mainly in the channel flow direction. As the water level in the main channel drops and the flow occupies only a fraction of the breach section, erosion is further concentrated at the downstream breach toe, triggering side slope collapses. The eroded material is then transported by the breach flow causing successive slope collapses, thereby controlling the breach widening.

### 4.1.2. Breach Side Slopes

As shown in Figure 4a, the longitudinal breach profiles are characterized by a slope change at locations closely coinciding with the water surface. This slope change was also observed by *Spinewine et al.* [2004]
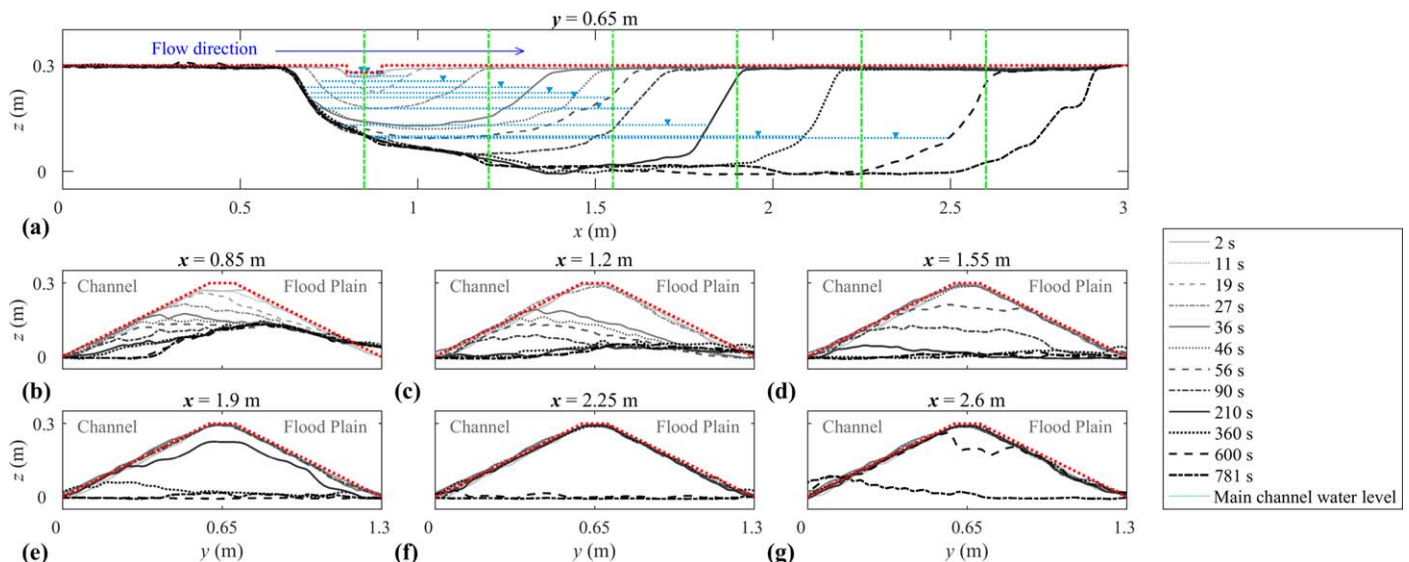


**Figure 4.** Breach geometry evolution for Test 8. (a) Longitudinal profiles at dike crest and (b–g) cross sections along the dike centerline axis.
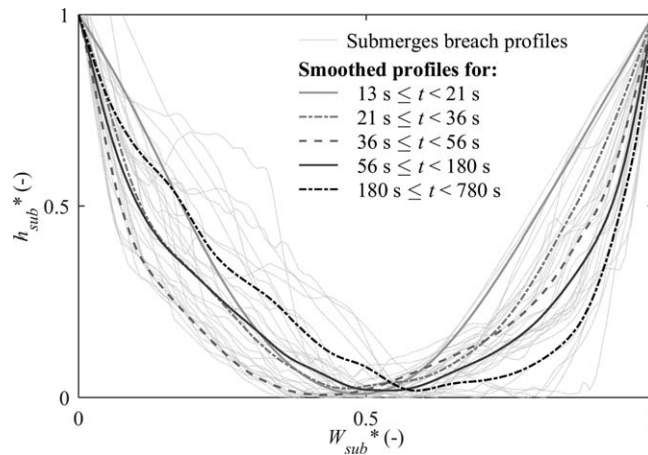
**Figure 5.** Normalized profiles of the submerged breach for Test 8.

and *Frank and Hager* [2016] for frontal dike experiments with a falling reservoir water level. The emerged part of the breach sides is steeper because the sand particles are sealed by apparent cohesion induced by negative pore water pressure [*Wei et al.*, 2016]. The side slope angles (from 41° to 59° for the Test 8) exceed the angle of repose of sediment ($\varphi_{sand} \approx 33°$). The submerged breach portion displays mild slopes and a nearly parabolic shape. This is consistent with the observations of *Coleman et al.* [2002] for frontal dike breach experiments with a constant reservoir level and by *Frank and Hager* [2016] with a falling reservoir water level.

Figure 5 shows the submerged breach shape development for Test 8. In this figure, $h_{sub}* = (z - z_{sub,min})/(z_{sub,max} - z_{sub,min})$ is the normalized breach depth and $W_{sub}^{}* = (x - x_{sub,min})/(x_{sub,max} - x_{sub,min})$ is the normalized breach width, with $z_{sub,min}$ as the breach invert elevation, 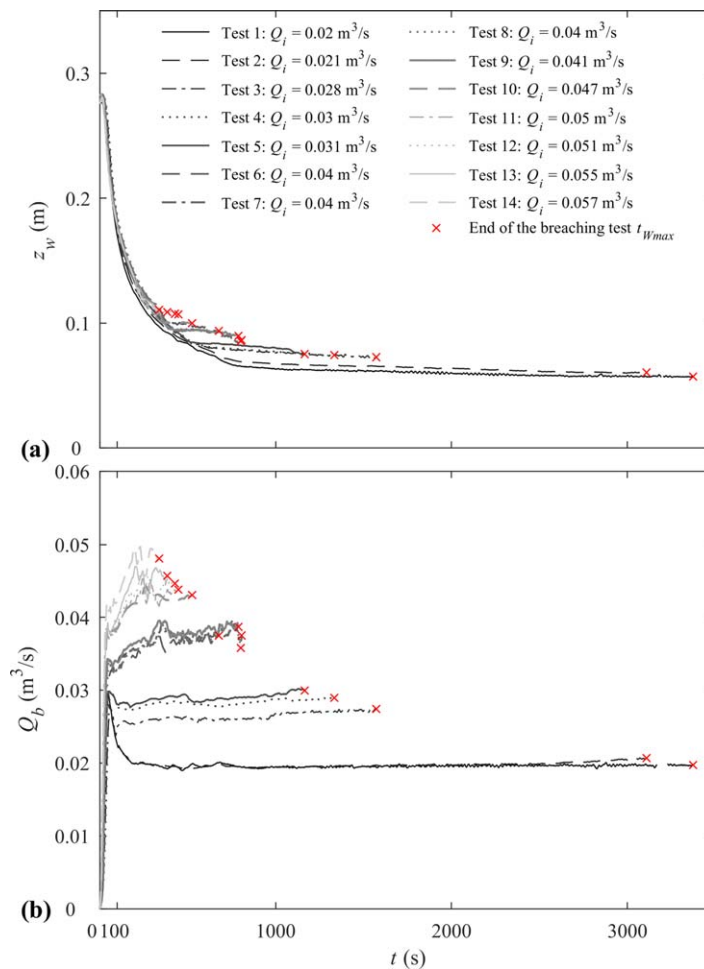$z_{sub,max}$ the elevation of the highest point of the submerged breach, $x_{sub,min}$ and $x_{sub,max}$ $x$ coordinates of the starting and ending points of the submerged breach, respectively. One can see that the shape of the submerged part of the breach is not symmetric but more tilted toward the channel downstream end, reflecting the signature of asymmetric distribution of the flow velocities. This difference in slope angles underlines the influence of the water level in the breach evolution. Compared to a falling channel water level case, constant or nearly constant channel water levels are expected to induce wider breaches.

### 4.2. Influence of Inflow Discharge
### 4.2.1. Breach Discharge and Water Level

Figure 6 shows the evolution of the water level in the main channel and the breach hydrograph for Tests 1–14. In all tests, the water level behaves similarly, slightly rising initially due to channel filling ($Q_i > Q_b + Q_o$). The breach expansion quickly takes place and flow conveyance increases so that the
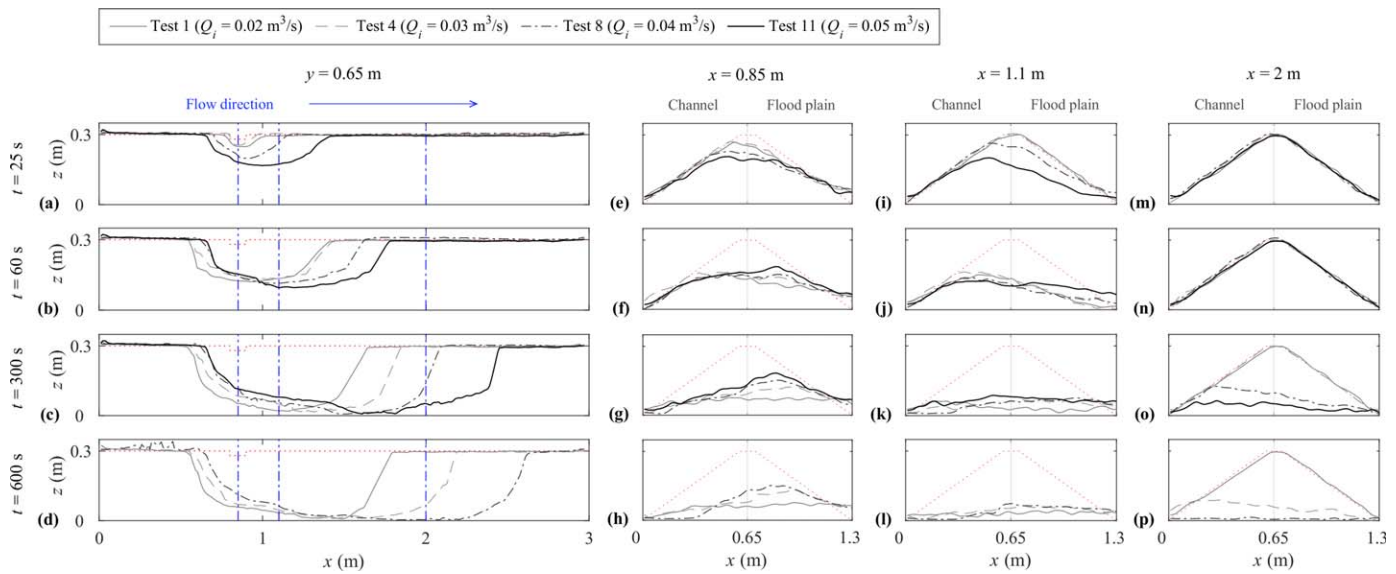


**Figure 6.** Results for Tests 1–14. (a) Water level evolution in main channel and (b) breach flow hydrograph.

**Figure 7.** Evolution of longitudinal and transversal breach profiles. Red dotted lines indicate initial dike shape and blue dash-dotted lines indicate cross sections. Test 11 ended at $t = 481$ s.

channel water level drops ($Q_i < Q_b + Q_o$). The evolution of the mean channel water level $z_w$ shows a low sensitivity to $Q_i$ over the first 340 s because the free surface drops at approximately the same rate in all tests (Figure 6a). For a lower discharge $Q_i$ (e.g., Tests 1–5), the water level stabilizes around an equilibrium value corresponding to the critical flow regime, whereas in tests with higher inflow discharges (e.g., Tests 6–10) a steady or quasi-steady state is not observed because the limits of the breach expansion are reached.

A fast rise of the breach discharge is noted during the first minute in all tests, followed by a stabilization of the breach discharge to its final value (Figure 6b). The gap between $Q_i$ and $Q_b$ at test end ($t = t_{Wmax}$) increases as $Q_i$ increases. This is due to the approach flow velocity $V_i$ in front of the breach [*Hager*, 1987; *Borghei et al.*, 1999] ($V_i = 0.75$ m/s for $Q_i = 0.020$ m$^3$/s (Test 1) and $V_i = 1.14$ m/s for $Q_i = 0.057$ m$^3$/s (Test 14) at $t = t_{Wmax}$) as well as to the downstream boundary condition [*Rifai et al.*, 2016c]. A correlation between $t_{Wmax}$ and $Q_i$ is noted. The maximum observable breach width $l_{b,max}$ is reached after a much longer time as $Q_i$ decreases.

### 4.2.2. Breach Evolution

Figure 7 shows the longitudinal and transversal breach profiles at different times for Tests 1, 4, 8, and 11. The breach evolution dynamics are strongly affected by $Q_i$ (Figures 7a–7d). The flow velocity in the main channel affects greatly the breach growth and duration, especially the widening process due to slope failure. The breach widens faster for tests with higher $Q_i$ values. Increasing $Q_i$, the breach side shape undergoes a higher erosion on the downstream breach side (Figures 7e–7p). Because the evolution of the water level in the main channel remains independent of $Q_i$ over the first 340 s (Figure 6a), changes in the breach shape as a function of $Q_i$ cannot be explained by the evolution of the main channel water level. This suggests that the flow momentum in the main channel is the principal cause of the differences in the dynamics of the breach widening for the tests conducted with different inflow discharges.

### 4.2.3. Final Breach State

Tests were stopped once erosion extended over the rigid dike part. Because sand has a low resistance against erosion, the breach development provides a direct feedback of the prevailing flow field in the breach vicinity. Figure 8 shows the 3-D reconstructed DEMs of the final breach and the corresponding times for selected tests. The time to reach the maximum breach width changes significantly with the inflow discharge, i.e., an increase by 150% of $Q_i$ induces a breach 7 times faster.

The 3-D breach shape is also affected. For each final DEM the *breach channel principal axis* was visually identified. For lower inflow discharge ($Q_i = 0.02$ m$^3$/s), this is deviated by an angle $\theta \approx 53°$ relative to the dike axis, increasing as $Q_i$ increases, e.g., $\theta \approx 60°$, $83°$, and $98°$ for $Q_i = 0.03$, $0.04$, and $0.05$ m$^3$/s, respectively. For the latter case ($Q_i = 0.05$ m$^3$/s), the breach discharge orientation leans toward the upstream side of the
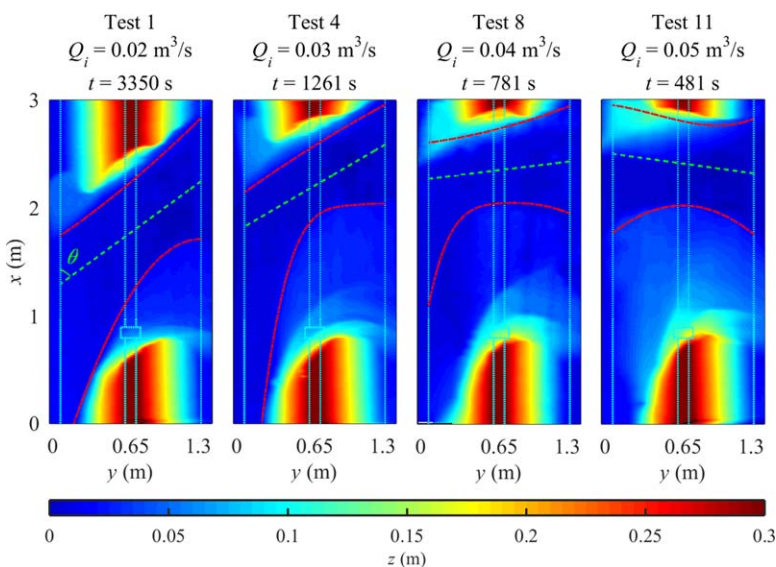
**Figure 8.** Final breach for different inflow discharges. Blue dotted lines indicate initial dike shape; red dash-dotted line, delimitates main breach channel; and green dashed lines indicate breach channel principal axis.

channel ($\theta > 90°$) and erosion of the channel side is observed at the downstream dike end. These $\theta$ values differ from analogous general observations on side weir outflows, where the corresponding lateral outflow angle $\phi$ is expressed as $\sin \phi = [(Z_w - W)/(3 - 2 Z_w - W)]^{0.5}$ with $Z_w = z_w/H$ and $W = w/H$, with $w$ as the weir crest height and $H$ the energy head in the main channel [*Hager*, 1987]. As the approach flow velocity increases, $H$ increases so that $\phi$ decreases.

For experiments with $Q_i$ ranging between 0.02 and 0.05 m³/s, the lateral outflow angles are estimated to $\phi \approx 55°$, which agrees well with the deviation angle of the breach principal axis $\theta$ for Tests 1 and 4 but not for Tests 8 and 11. Tests 1 and 4 differ from Tests 8 and 11 mainly because the breach width was almost stabilized at test end for the former, while in the latter the test was interrupted because the nonerodible part of the dike was reached. This may explain the differences in deviation angles of the breach principal axis.

### 4.3. Influence of the Downstream Boundary Condition
### 4.3.1. Breach Discharge and Water Level

Three additional tests were conducted with the same inflow discharge ($Q_i \approx 0.04$ m³/s) using different downstream regulating systems: Test 15 with a sluice gate and Tests 16 and 17 with a rectilinear weir. They are compared to Tests 6–9 conducted with the perforated plane. Only slight differences are noted for the evolution of the main channel water level (Figure 9a). The rectilinear weir condition leads to slightly higher water levels (Tests 16 and 17) than those obtained with the perforated plate (Tests 6–9), whereas the sluice gate (Test 15) leads to the lowest water levels. This is in agreement with the rating curves, because for $Q_o < Q_i$, the main channel water level ranks from the highest to the lowest for the rectilinear weir, the perforated plane and the sluice gate, respectively.

The larger overtopping depth observed for the rectilinear weir is explained by the filling time of the channel. Changing from the filling inflow discharge $Q_{i0}$ to its finale value $Q_i$, the channel water level reaches the dike crest level in 6, 10, and 18 s for the rectilinear weir, the perforated plane and the sluice gate, respectively. The adaptation of the channel water level in the rectilinear weir configuration causes an increased initial overtopping over the notch.

The breach hydrographs show significant differences (Figure 9b). Using the rectilinear weir, the maximum breach discharge exceeds $Q_i$ by 30%. The final breach discharges represent about 95–100% of $Q_i$ in tests with the rectilinear weir and perforated plane, respectively, but only 62% of $Q_i$ for the sluice gate test. While the channel main water levels are similar, these significant differences in the breach hydrograph reflect in reality differences in the breach dimensions and development.
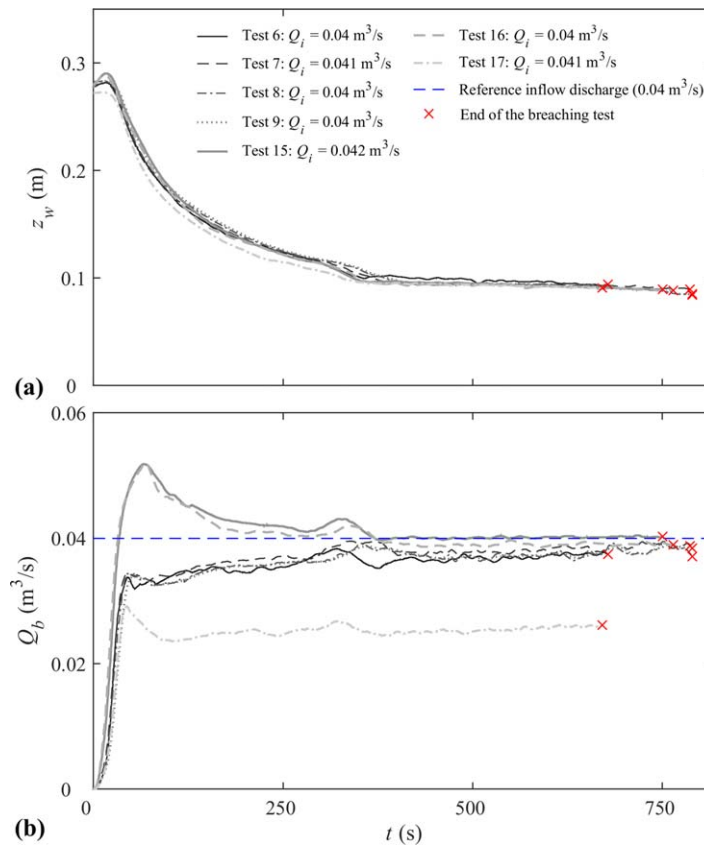
**Figure 9.** Comparison of (a) main channel water levels and (b) breach hydrographs.

### 4.3.2. Breach Evolution

The longitudinal and transversal breach profiles are significantly influenced by the downstream boundary condition (Figure 10). Over the first 300 s, the breach widening is faster for the rectilinear weir. This is consistent with the larger overtopping shown in Figure 9a, leading to wider submerged parts of the breach and an accelerated erosion of the breach side generated by the lower value of the submerged angle of repose of sand.

Using the sluice gate, a slower breach expansion during the first 60 s is observed, whereas it leads afterward to a wider breach than in the other tests (Figures 10c and 10d). Because the evolution of the main channel water level remains almost the same in all tests, the observed differences in breach widening dynamics result from differences in the flow momentum in the main channel. Indeed, at $t = 600$ s, flow velocity in the main channel downstream of the breach $V_o$ is 0, 0.052, and 0.38 m/s for the rectilinear weir, the perforated plane and the sluice gate, respectively.

The longitudinal breach profiles reveal differences in the breach widening toward upstream that takes place over the first 60 s and hardly evolves afterward. The maximum and minimum upward erosion depths are
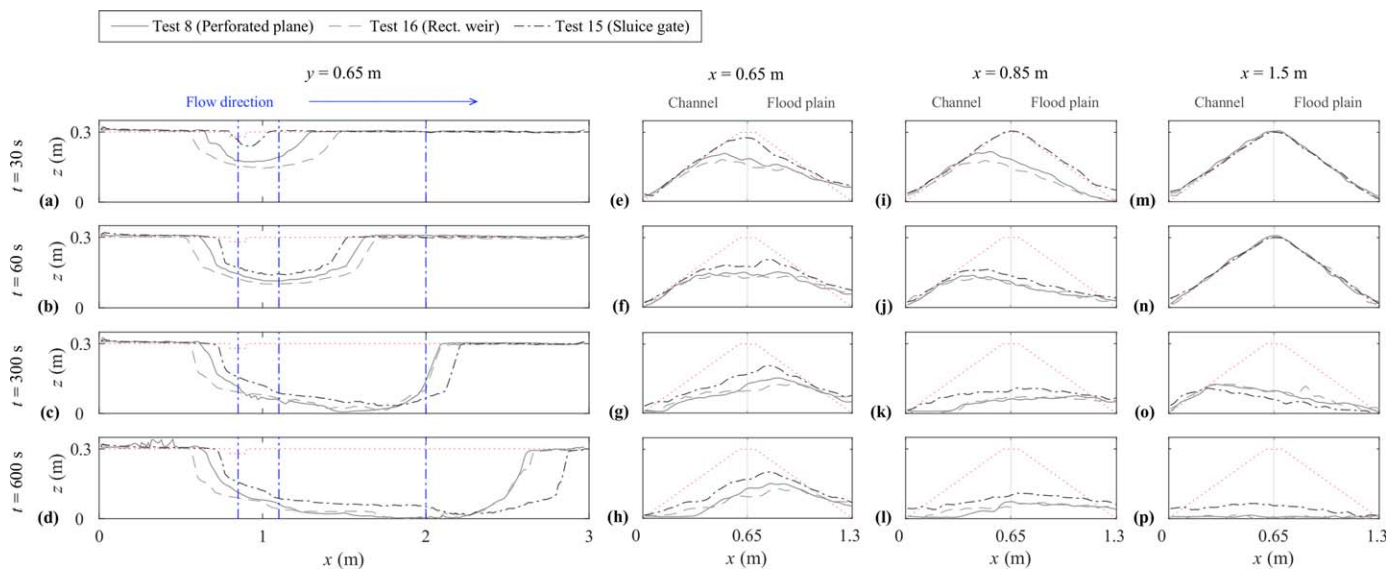


**Figure 10.** Evolution of longitudinal and transversal breach profiles for different downstream regulating systems. Red dotted lines indicate initial dike shape and blue dash-dotted lines indicate location of cross sections.
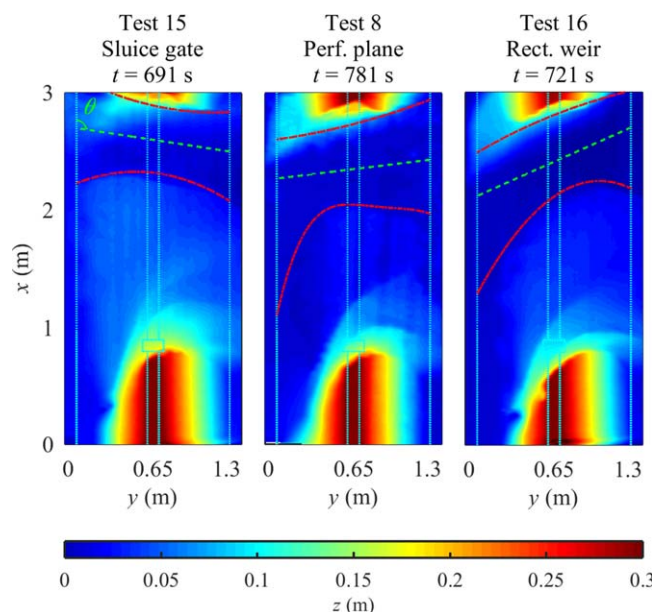
**Figure 11.** Final breach shapes according to different downstream boundary regulating system. Blue dotted lines indicate initial dike shape; red dash-dotted line, main breach channel; and green dashed lines indicate principal breach channel axis.

observed for the rectilinear weir and for the sluice gate, respectively. This results from the larger overtopping observed for the rectilinear weir, enhancing the breach widening symmetrically, i.e., both upstream and downstream, as in the frontal configuration. In contrast, the larger final breach width observed with the sluice gate results from the effect of a higher flow momentum in the main channel, causing a nonsymmetric breach expansion toward the downstream end of the channel.

The cross-sectional profiles at $x = 0.65$ m (Figures 10e–10h) provide insight into the 3-D breach development. Although the upstream channel velocities are identical for the three tests, the rectilinear weir case generates more erosion of the upstream channel side caused by the accelerated flow deviating toward the breach. During the first 60 s, upward erosion of the channel face is restricted to an upper dike portion (Figure 10f), confirming that this erosion is caused by the flow deviated toward the breach and not by higher flow velocities in the upstream main channel part. Cross sections at $x = 0.85$ and 1.5 m (Figures 10i–10p) reveal a delayed breach deepening for the sluice gate test, in which more widening takes place at the expense of breach deepening due to the specific flow configuration.

### 4.3.3. Final Breach State
The final breach shapes display significant differences (Figure 11). Using the sluice gate, these are similar to those with the perforated plane and an inflow discharge 25% higher (Figure 8). The relatively high flow velocity in the downstream part of the main channel maintains a continuous breach widening toward downstream. In addition, eroded material from the upstream dike channel side is deposited at the upstream side of the breach forming a sediment layer, so that the breach flow becomes more concentrated toward the downstream breach side. Both tests with the rectilinear weir lead to a dead end configuration [*Hager and Volkart*, 1986] once the channel water level drops below the weir crest ($z_w < 0.225$ m at $t \approx 60$ s). This prevents erosion to progress toward downstream.

Values of the breach channel deviation angle ($\theta \approx 99°$, $83°$, and $66°$ for the sluice gate, the perforated plane, and the rectilinear weir, respectively) agree with the previous observations on the final breach geometries obtained with different values of $Q_i$ and the ranking of the downstream regulating systems according to their tendency to promote of the downward widening.

## 5. Conclusions

Laboratory experiments were conducted on overtopping failure of noncohesive fluvial sand dikes accounting for a flow parallel to the dike axis. The breach geometry evolution was monitored using laser profilometry. Tests unveiled the processes underpinning overtopping induced fluvial dike failure.

Results show that upward breach widening is caused by two mechanisms: (1) flow acceleration in the main channel triggering erosion of the upstream channel side of the dike, weakening its profile and generating breach widening by wedge collapse and (2) acceleration of flow in the main channel deviating toward the breach and of flow across the breach. The breach invert level limits the erosion amplitude, causing the so-called breach *hour glass shape* usually reported for the noncohesive dam breach. The downward breach

widening is due to (1) erosion of submerged breach part induced by flow across the breach. This erosion occurs preferentially toward downstream as main channel flow velocity increases; (2) erosion at downstream breach toe, generating breach downstream side collapse. The slumped material is eroded and so forth.

The upward and downward breach widenings were found to be highly dependent on the downstream boundary condition (i.e., perforated plane, rectilinear weir, or sluice gate) in the main channel. The breach (quasi-) stabilization is signaled by the alignment of its principal axis with the theoretical value of flow deviation angle. Overall, these peculiarities are to be accounted for in the prediction of the breach evolution as classical dam breach models do not account for the main channel flow momentum.

The direction and shape of breach progression should be taken into account to target dike inspection, emergency closure and measures to limit dike breach, and tactical blowing up of dike (e.g., fuse plug).

The present study is an addition to existing works performed for dam breach configurations. Further laboratory tests are ongoing, covering a broader range of main channel, floodplain and dike dimensions as well as dike material. Data will be used to assess the applicability of different types of breach model (i.e., simple empirical formulas, predictive physically based models) to compute breach growth in fluvial dike configurations.

## Notation

| | |
|---|---|
| $A_{mc}$ | cross-sectional main channel flow area, $m^2$. |
| $A_{Gi}$ | flow surface area associated to gauge station $G_i$, $m^2$. |
| $d_i$ | grain size such that i% of the sample is finer than $d_i$. |
| $\mathbf{F}_i$ | Froude number in main channel prior to overtopping. |
| $g$ | gravity acceleration, m s$^{-2}$. |
| $H$ | energy head, m. |
| $h_d$ | dike height, m. |
| $h_{sub}*$ | normalized breach depth. |
| $l_{b,max}$ | maximum observable breach width, m. |
| $l_{dc}$ | dike crest width, m. |
| $L_d$ | dike length, m. |
| $l_d$ | dike width, m. |
| $l_{mc}$ | main channel width, m. |
| $L_{mc}$ | main channel length, m. |
| $p$ | porosity. |
| $Q_b$ | breach discharge, m$^3$ s$^{-1}$. |
| $Q_d$ | drainage discharge, m$^3$ s$^{-1}$. |
| $Q_i$ | channel inflow discharge, m$^3$ s$^{-1}$. |
| $Q_{i0}$ | channel filing inflow discharge, m$^3$ s$^{-1}$. |
| $Q_o$ | channel outflow discharge, m$^3$ s$^{-1}$. |
| $S_i, S_o$ | dike side slopes (channel side and floodplain side, respectively). |
| $t$ | time, s. |
| $t_{Wmax}$ | breach experiment end time, s. |
| $V_i$ | upstream flow velocity, m s$^{-1}$. |
| $V_o$ | downstream flow velocity, m s$^{-1}$. |
| $w$ | side weir crest height, m. |
| $W_{sub}*$ | normalized breach width. |
| $W$ | $w/H$. |
| $x_{sub,min}$ | x coordinate of the beginning of the submerged part of the breach. |
| $x_{sub,max}$ | x coordinate of the end of the submerged part of the breach. |
| $z_{Gi}$ | water level at gauge $G_i$, m. |
| $z_{sub,max}$ | elevation of the highest submerged point of the breach, m. |
| $z_{sub,min}$ | elevation of the breach invert, m. |

| | |
|---|---|
| $z_w$ | averaged water level, m. |
| $Z_w$ | $z_w/H$. |
| $\theta$ | breach channel deviation angle, m. |
| $\rho_b$ | bulk density, kg m$^{-3}$. |
| $\rho_s$ | sand density, kg m$^{-3}$. |
| $\sigma$ | sorting coefficient. |
| $\varphi_{sand}$ | sand angle of repose, °. |
| $\phi$ | side flow deviation angle, °. |

## References

Al-Riffai, M. (2014), Experimental study of breach mechanics in overtopped noncohesive earthen embankments, PhD thesis, Univ. of Ottawa, Ottawa.

Apel, H., B. Merz, and A. H. Thieken (2009), Influence of dike breaches on flood frequency estimation, *Comput. Geosci.*, *35*(5), 907–923.

ASCE/EWRI Task Committee on Dam/Levee Breaching (2011), Earthen embankment breaching, *J. Hydraul. Eng.*, *137*(12), 1549–1564.

Bhattarai, P. K., H. Nakagaw, K. Kawaike, and J. Zhang (2015), Study of breach characteristics and scour pattern for overtopping induced river dyke breach, paper presented at 36th IAHR World Congress, International Association for Hydro-Environment Engineering and Research (IAHR), The Hague, Netherlands.

Borghei, S. M., M. R. Jalili, and M. Ghodsian (1999), Discharge coefficient for sharp-crested side weir in subcritical flow, *J. Hydraul. Eng.*, *125*(10), 1051–1056.

Charrier, G. (2015), Etude expérimentale des ruptures de digues fluviales par surverse [Experimental study of river dikes breaching by over-topping], PhD thesis, Aix-Marseille Univ., Marseille, France.

Chinnarasri, C., S. Jirakitlerd, and S. Wongwises (2004), Embankment dam breach and its outflow characteristics, *Civ. Eng. Environ. Syst.*, *21*(4), 247–264.

Coleman, S. E., D. P. Andrews, and M. G. Webby (2002), Overtopping breaching of noncohesive homogeneous embankments, *J. Hydraul. Eng.*, *128*(9), 829–838.

Dou, S. T., D. W. Wang, M. H. Yu, and Y. J. Liang (2014), Numerical modeling of the lateral widening of levee breach by overtopping in a flume with 180° bend, *Nat. Hazards Earth Syst. Sci.*, *14*, 11–20.

Frank, P.-J., and W. H. Hager (2015), Spatial dike breach: Sediment surface topography using photogrammetry, paper presented at 36th IAHR World Conference, The Hague, Netherlands.

Frank, P.-J., and W. H. Hager (2016), Challenges of dike breach hydraulics, paper presented at the 8th International Conference on Fluvial Hydraulics (River Flow), International Association for Hydro-Environment Engineering and Research (IAHR), Saint Louis, Mo.

Froehlich, D. C. (2008), Embankment dam breach parameters and their uncertainties, *J. Hydraul. Eng.*, *134*(12), 1708–1721.

Fry, J., A. Vogel, P. Royet, and J. Courivaud (2012), Dam failures by erosion: Lessons from ERINOH data bases, paper presented at the 6th International Conference on Scour and Erosion, International Association for Hydro-Environment Engineering and Research (IAHR), Paris.

Glassner, A. S. (1989), *An Introduction to Ray tracing*, 328 pp., International Society for Soil Mechanics and Foundation Engineering (ISSMGE), Elsevier Sci., London.

Hager, W. H. (1987), Lateral outflow over side weirs, *J. Hydraul. Eng.*, *113*(4), 491–504.

Hager, W. H., and P. U. Volkart (1986), Distribution channels, *J. Hydraul. Eng.*, *112*(10), 935–952.

Hui, R., E. Jachens, and J. Lund (2016), Risk-based planning analysis for a single levee, *Water Resour. Res.*, *52*, 2513–2528, doi:10.1002/2014WR016478.

IPCC (2014), *Climate Change 2014—Impacts, Adaptation and Vulnerability: Regional Aspects*, 688 pp., Cambridge Univ. Press, United Kingdom and New York, N. Y.

Islam, S. (2012), Study on levee breach and successive disasters in low-land through numerical and experimental approaches, PhD thesis, Nagoya Univ., Nagoya, Japan.

Jandora, J., and J. Říha (2008), *The Failure of Embankment Dams due to Overtopping*, Vutium, Brno, CZ.

Kakinuma, T., and Y. Shimizu (2014), Large-scale experiment and numerical modeling of a riverine levee breach, *J. Hydraul. Eng.*, *140*(9), 1–9.

Madsen, H., D. Lawrence, M. Lang, M. Martinkova, and T. R. Kjeldsen (2014), Review of trend analysis and climate change projections of extreme precipitation and floods in Europe, *J. Hydrol.*, *519*(D), 3634–3650.

Michelazzo, G. (2014), Breaching of river levees: Analytical flow modelling and experimental hydro-morphodynamic investigations, PhD thesis, Univ. of Florence, Florence, Italy.

Morris, M., M. A. A. M. Hassan, A. Kortenhaus, and P. Visser (2009), *Breaching Processes: A State of the Art Review. FLOODsite Project Report*, HR Wallingford, Wallingford, U. K.

Morris, M. W., M. A. A. M. Hassan, and K. A. Vaskinn (2007), Breach formation: Field test and laboratory experiments, *J. Hydraul. Res.*, *45*, suppl. 1, 9–17.

Nakagawa, H., H. Mizutani, K. Kawaike, H. Zhang, Y. Yoden, and B. Shrestha (2013), Numerical modelling of erosion of unsaturated river embankment due to overtopping flow, paper presented at the 12th International Symposium on River Sedimentation (ISRS), IRTCES, Kyoto, Japan.

Orendorff, B., M. Al-Riffai, I. Nistor, and C. Rennie (2013), Breach outflow characteristics of non-cohesive embankment dams, *Can. J. Civ. Eng.*, *40*(3), 243–253.

Orlandini, S., G. Moretti, and J. D. Albertson (2015), Evidence of an emerging levee failure mechanism causing disastrous floods in Italy, *Water Resour. Res.*, *51*, 7995–8011, doi:10.1002/2015WR017426.

Pickert, G., V. Weitbrecht, and A. Bieberstein (2011), Beaching of overtopped river embankments controlled by apparent cohesion, *J. Hydraul. Res.*, *49*(2), 143–156.

Powledge, G. R., D. C. Ralston, P. Miller, Y. H. Chen, P. E. Clopper, and D. M. Temple (1989), Mechanics of overflow erosion on embankments. I: Research activities, *J. Hydraul. Eng.*, *115*(8), 1040–1055.

Pugh, C. A. (1985), Hydraulic model studies of fuse plug embankments, report REC-ERC-85-7, U.S. Dep. of the Inter., Bur. of Reclam, Denver, Colo.

Rifai, I., S. Erpicum, P. Archambeau, M. Benoit, M. Pirotton, B. Dewals, and K. El Kadi Abderrezzak (2015), Physical modeling of lateral dike breaching due to overtopping, paper presented at 9th Symposium of River Coastal and Estuarine Morphodynamics (RCEM), International Association for Hydro-Environment Engineering and Research (IAHR), Iquitos, Peru.

Rifai, I., S. Erpicum, P. Archambeau, D. Violeau, M. Pirotton, B. Dewals, and K. El Kadi Abderrezzak (2016a), Sensitivity of the breaching process in the case of overtopping induced fluvial dike failure, paper presented at the 8th International Conference on Fluvial Hydraulics (River Flow), International Association for Hydro-Environment Engineering and Research (IAHR), Saint Louis, Mo.

Rifai, I., S. Erpicum, P. Archambeau, D. Violeau, M. Pirotton, K. El Kadi Abderrezzak, and B. Dewals (2016b), Monitoring topography of laboratory fluvial dike models subjected to breaching based on a laser profilometry technique, paper presented at the 13th International Symposium on River Sedimentation (ISRS), IRTCES, Stuttgart, Germany.

Rifai, I., S. Erpicum, P. Archambeau, D. Violeau, M. Pirotton, K. El Kadi Abderrezzak, and B. Dewals (2016c), Discussion of "Laboratory Study on 3D Flow Structures Induced by Zero-Height Side Weir and Implications for 1D Modeling" by Michelazzo G., H. Oumeraci, and E. Paris, *J. Hydraul. Eng.*, *143*(3), 1–1, doi:10.1061/(ASCE)HY.1943-7900.0001256.

Roger, S., B. J. Dewals, S. Erpicum, D. Schwanenberg, H. Schuttrumpf, J. Kongeter, and M. Pirotton (2009), Experimental and numerical investigations of dike-break induced flows, *J. Hydraul. Res.*, *47*(3), 349–359.

Rozov, A. L. (2003), Modeling a washout of dams, *J. Hydraul. Res.*, *41*(6), 565–577.

Schmocker, L. (2011), Application of a videometric measurement system to investigate spatial dike breach, in *Experimental Methods in Hydraulic Research, GeoPlanet: Earth Planet. Sci.*, vol. 1, pp. 247–254, Springer Sci. and Bus. Media, Dordrecht, The Netherlands.

Schmocker, L., and W. H. Hager (2009), Modelling dike breaching due to overtopping, *J. Hydraul. Res.*, *47*(5), 585–597.

Schmocker, L., and W. H. Hager (2012), Plane dike-breach due to overtopping: Effects of sediment, dike height and discharge, *J. Hydraul. Res.*, *50*(6), 576–586.

Simmler, H., and L. Samet (1982), Dam failure from overtopping studied on a hydraulic model, paper presented at the 14th Congress of the International Commission on Large Dams, Icold, Rio de Janeiro, Brazil.

Singh, V. (1996), *Dam Breach Modeling Technology*, Springer Sci. and Bus. Media, Dordrecht, The Netherlands.

Spinewine, B., A. Delobbe, L. Elslander, and Y. Zech (2004), Experimental investigation of the breach growth process in sand dikes, paper presented at the 2nd International Conference on Fluvial Hydraulics (River Flow), International Association for Hydro-Environment Engineering and Research (IAHR), Naples, Italy.

Tabrizi, A. A., E. Elalfy, L. Ann LaRocque, M. H. Chaudhry, and J. Imran (2015), Experimental modeling of levee failure process due to overtopping, paper presented in Annual Meeting of Association of State Dam Safety Officials (ASDSO), Association of State Dam Safety Officials (ASDSO), New Orleans, La.

Tabrizi, A. A., E. Elalfy, M. Elkholy, M. H Chaudhry, and J. Imran (2016), Effects of compaction on embankment breach due to overtopping, *J. Hydraul. Res.*, *55*, 236–247.

Visser, P. J. (1998), Breach growth in sand-dikes, PhD thesis, TU Delft, Delft, Netherlands.

Vorogushyn, S., B. Merz, K. E. Lindenschmidt, and H. Apel (2010), A new methodology for flood hazard assessment considering dike breaches, *Water Resour. Res.*, *46*, W08541, doi:10.1029/2009WR008475.

Wahl, T. (2004), Uncertainty of predictions of embankment dam breach parameters, *J. Hydraul. Eng.*, *130*(5), 389–397.

Wahl, T., and D. Lentz (2012), Experimental methods for studying canal breach processes, paper presented at Hydraulic Measurements and Experimental Methods Conference (HMEM), American Society of Civil Engineers (ASCE) - Environmental and Water Resources Institute (EWRI), Snowbird, Utah.

Wei, H., M. Yu, D. Wang, and Y. Li (2016), Overtopping breaching of river levees constructed with cohesive sediments, *Nat. Hazards Earth Syst. Sci.*, *16*(7), 1541–1551.

Wu, W., R. Marsooli, and Z. He (2012), Depth-averaged two-dimensional model of unsteady flow and sediment transport due to noncohesive embankment break/breaching, *J. Hydraul. Eng.*, *138*(6), 503–516.

Zhang, J., Y. Li, G. Xuan, X. Wang, and J. Li (2009), Overtopping breaching of cohesive homogeneous earth dam with different cohesive strength, *Sci. China, Ser. E: Technol. Sci.*, *52*(10), 3024–3029.

Zhu, Y., P. J. Visser, J. K. Vrijling, and G. Wang (2011), Experimental investigation on breaching of embankments, *Sci. China, Ser. E: Technol. Sci.*, *54*(1), 148–155.